Supporting Information for

The impact of framework flexibility and defects on the water adsorption in CAU-10-H

Ivan V. Grenev[1,2,*], Aleksandr A. Shubin[1,2], Marina V. Solovyeva[1] and Larisa G. Gordeeva[1]

(1) Boreskov Institute of Catalysis, Ac. Lavrentiev av. 5, Novosibirsk 630090, Russia

(2) Novosibirsk State University, Pirogova str. 1, Novosibirsk 630090, Russia

* - author for correspondence, greneviv@catalysis.ru

Contents:

Section S1. VASP and REPEAT calculation details

All density functional theory (DFT) calculations were performed using the Vienna Ab Initio Simulation Package (VASP version 5.4.4)[1,2]. The interaction between ions and electrons was described by the projector-augmented wave (PAW) method allowing to compute an approximate all-electron wave function for non-core electrons[3,4]. The Generalized Gradient Approximation (GGA) under the Perdew, Burke, and Ernzerhof (PBE) exchange-correlation functional[5] was applied for all calculations. A plane wave kinetic cutoff energy of 450 eV was used in all calculations. Zero damping DFT-D3 method of Grimme[6] was applied to account for Van der Waals interactions[7,8]. The unit size was chosen equal to 21.52 × 21.52 × 10.32 Å. The Monkhorst– Pack scheme[9] (2 × 2 × 4 mesh of *k*-points) was used for the numerical integration over the Brillouin zone. For the threshold of 10^{-6} eV, set for the electronic relaxation, any movement of the ions was stopped if the change in the total (free) energy was smaller than 10^{-5} eV between two ionic relaxation steps. For the optimized structures, the electrostatic potentials were calculated with the above parameters using the LVHAR = 1 option in the VASP package. Effective atomic charges were obtained from these potentials using the Repeating Electrostatic Potential Extracted ATomic (REPEAT) calculations (with a real space cutoff radius of 10 Å and fast Fourier transform grid points of 300 × 300 × 144) as suggested by Woo and co-workers[10].

Section S2. Water model selection

There are numerous different water models that can be used to simulate the water adsorption in porous solids. The most widely used in the literature rigid nonpolarizable models are a 3-site model SPC/E[11], a family of 4-site models TIP4P (TIP4P[12], TIP4P/2005[13], TIP4P-Ew[14]) and a family of 5-site models TIP5P (TIP5P[15], TIP5P-Ew[16]). These models adequately predict the density and radial distribution function of liquid water. The Lennard-Jones (LJ) interaction potentials for all these models are very similar. Their main differences are related to the location of effective charges and the dipole moment. The model dipole moment in all these models is higher than that of water vapor and lower than that of liquid water. As a result, they do not predict the vapor–liquid equilibrium sufficiently well. For water adsorption in MOFs, the electrostatic interaction is the main adsorption factor. So, the choice of the water model will significantly affect the simulation results[17–19]. This problem could be solved by using polarizable models. However, it would cause a significant increase of the required computation time. In combination with additional computer performance requirements for account of the MOF flexibility during the simulation, the use of polarizable models is practically not possible.

Another important problem is substantial deviation of the predicted saturation pressure from the experimentally measured values. The experimental saturation pressure at 300 K is equal to 3576 Pa[20,21]. Meanwhile, according to the NIST Standard Reference SimulationWebsite[22], the saturation pressure at 300 K for models SPC/E, TIP4P and TIP4P/2005 are 1017 Pa, 5130 Pa and 802 Pa, correspondingly. These values were obtained using the grand-canonical Wang-Landau Monte Carlo method where LJ interactions were truncated at the cutoff radius 10 Å, with tail corrections and electrostatic interactions calculated using the Ewald summation technique. Note that the simulated saturation pressure can depend on the simulation conditions and the method used for the saturation pressure calculation. Due to significant differences of the simulated and experimental saturation pressure values, relative pressure P/P_0 rather than absolute pressure is usually used for comparison of experimental and simulated isotherms.

Table S1. Geometry and parameters of TIP4P water model.

r(OH), Å	∠(HOH), deg	r(OM), Å	ε/k_b, K	σ, Å	q(M)	q(H)
0.9572	104.52	0.15	78	3.154	-1.04	0.52

In this study the TIP4P model was used as the main water model. This model is the most successful in predicting the water adsorption for a series of MOFs[19,23–25]. The saturation pressure of the TIP4P model equal to 5130 Pa is closer to the experimental value in comparison with other popular models (for models SPC/E and TIP4P/2005 the simulated saturation pressure according

to NIST[22] differs from the experimental saturation pressure by factors of 3.5 and 4, respectively). The parameters of the TIP4P model are presented in Table S1.

Section S3. Water adsorption simulation details

The cumulative interaction potential was calculated as a sum of bonded (bond, bend, torsion and improper torsion) and non-bonded (LJ and electrostatic) interactions:

$$U_{\Sigma} = U_{bonded} + U_{nonbonded} \quad \text{S1}$$

The bonded and non-bonded potentials were described using the following functional forms:

$$U_{nonbonded} = U_{6-12} + U_{el} \quad \text{S2}$$

$$U_{bonded} = U_{bond} + U_{bend} + U_{torsion} + U_{imp.\ torsion} \quad \text{S3}$$

$$U_{bond} = \sum_{bonds} E_{bond}(r_{ij}) = \sum_{bonds} \frac{1}{2} k_{ij}(r_{ij} - r_{ij}^{0})^2 \quad \text{S4}$$

$$U_{bend} = \sum_{bends} E_{bend}(\theta_{ijk}) = \sum_{bends} \frac{1}{2} k_{ijk}(\theta_{ijk} - \theta_{ijk}^{0})^2 \quad \text{S5}$$

$$U_{torsion} = \sum_{torsions} E_{torsion}(\varphi_{ijkl}) = \sum_{torsions} k_{ijkl}(1 - Cos[2\varphi_{ijkl} - \varphi_{ijkl}^{0}]) \quad \text{S6}$$

$$U_{imp.\ torsion} = \sum_{imp.\ torsions} E_{imp.\ torsion}(\varphi_{ijkl}) = \sum_{imp.\ torsions} k_{ijkl}(1 - Cos[2\varphi_{ijkl} - \varphi_{ijkl}^{0}]) \quad \text{S7}$$

Table S2. Lennard-Jones parameters for the CAU-10-H atoms.

Atom Type	ε/k_B (K)	σ (Å)
Al	254.1	4.008
O1	78	3.154
Odef	78	3.154
O2	48.158	3.033
O3	48.158	3.033
C1	47.856	3.473
C2	47.856	3.473
C3	47.856	3.473
C4	47.856	3.473
C5	47.856	3.473
H1	0	2.846
Hdef	0	2.846
H2	7.649	2.846
H3	7.649	2.846
H4	7.649	2.846

Table S3. Bond stretch parameters.

Atom Types		k_{ij}/k_B (K/Å^2)	r_{ij}^0 (Å)
C1	C2	483414	1.396
C1	C3	483414	1.403
C3	C4	483414	1.393
C1	C5	353750	1.490
C2	H2	366000	1.091
C3	H3	366000	1.091
C4	H4	366000	1.091
O1	H1	352780	0.972
O_def	H_def	352780	0.974

Table S4. Bond angle bending parameters.

Atom Types			k_{ijk}/k_B (K/rad^2)	θ_{ijk}^0 (deg)
C1	C2	C1	90640	120
C1	C3	C4	90640	120
C3	C1	C2	90640	120
C3	C4	C3	90640	120
C5	C1	C2	90640	120
C5	C1	C3	90640	120
C1	C3	H3	37263	120
C1	C2	H2	37263	120
C3	C4	H4	37263	120
C4	C3	H3	37263	120

Table S5. Torsion interaction parameters.

Atom Types				k_{ijkl}/k_B (K)	φ_{ijkl}^0 (deg)
C5	C1	C3	C4	1511	0
C5	C1	C2	C1	1511	0
C1	C2	C1	C3	1511	0
C1	C3	C4	C3	1511	0
C2	C1	C3	C4	1511	0
H2	C2	C1	C5	1511	0
H2	C2	C1	C3	1511	0
H3	C3	C4	H4	1511	0
H3	C3	C4	C3	1511	0
H3	C3	C1	C5	1511	0
H3	C3	C1	C2	1511	0
H4	C4	C3	C1	1511	0

Table S6. Improper torsion interaction parameters.

Atom Types				k_{ijkl}/k_B (K)	φ_{ijkl}^0 (deg)
C1	C3	C4	H3	186.3	0
C3	C4	C3	H4	186.3	0
C1	C2	C1	H2	186.3	0
C5	C1	C3	C2	5035.6	0

Section S4. Adsorption surfaces

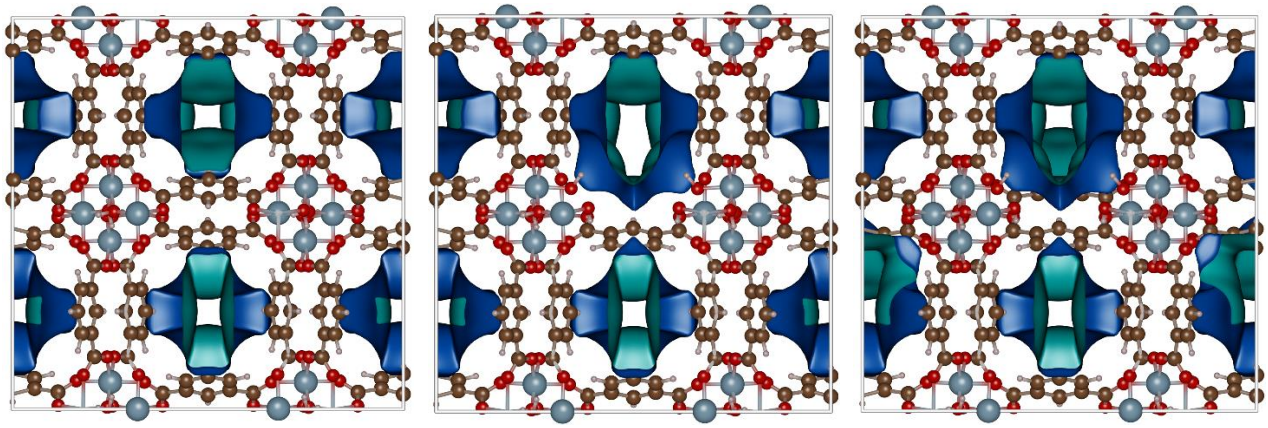

a b c

Figure S1. Adsorption surfaces for the rigid ideal model (a), the rigid uniform defective model (b) and the rigid mixed defective model (c) of the CAU-10-H structure.

Section S5. Radial distribution functions and simulation snapshots of adsorption

Rigid ideal CAU-10-H structure

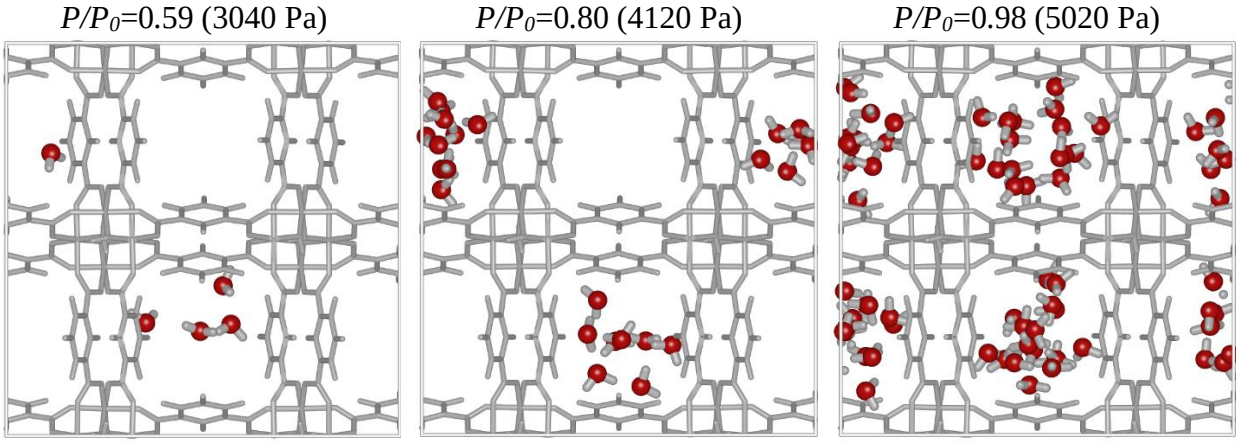

Figure S2. Simulation snapshots of water adsorption in rigid ideal CAU-10-H structure.

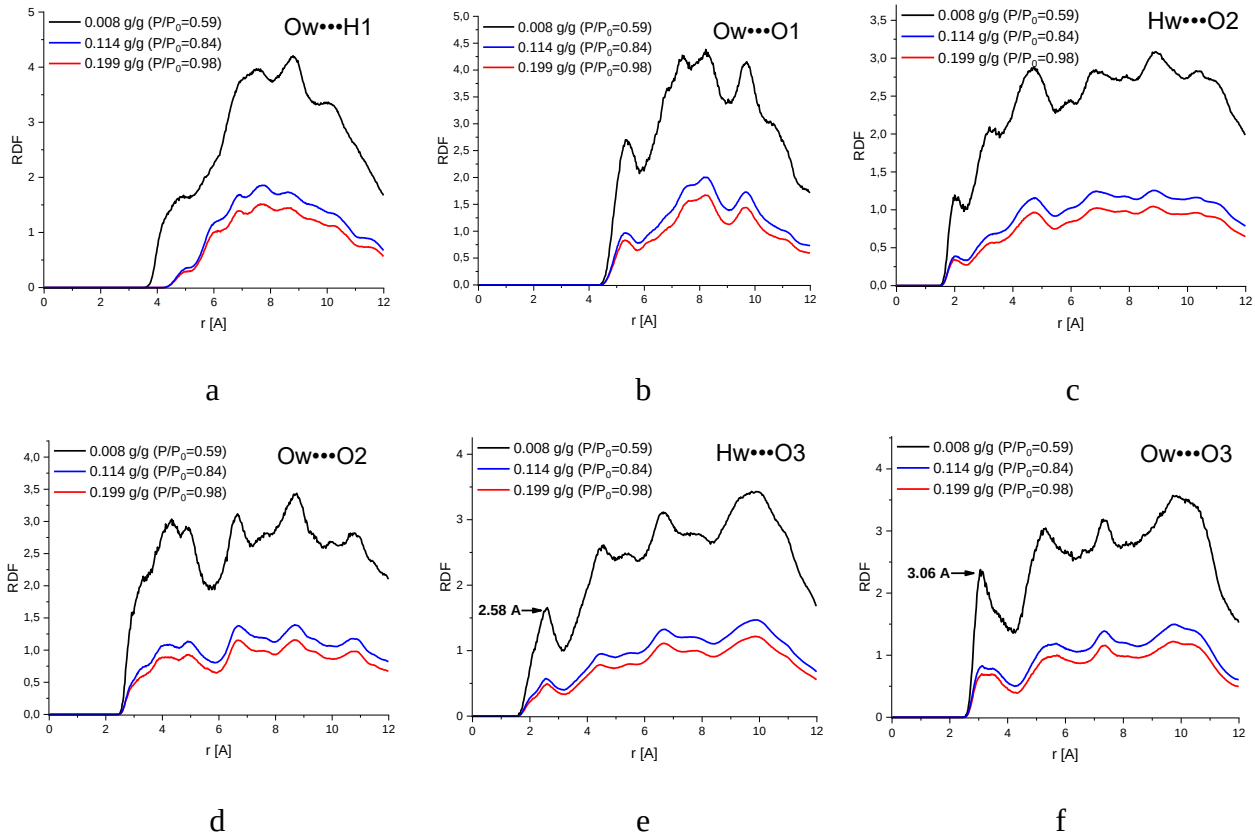

Figure S3. Radial distribution functions in rigid ideal CAU-10-H structure: Ow···H1 (a), Ow···O1 (b), Hw···O2 (c), Ow···O2 (d), Hw···O3 (e) and Ow···O3 (f). The notation of the CAU-10-H structures is presented in Figure 2.

Flexible ideal CAU-10-H structure

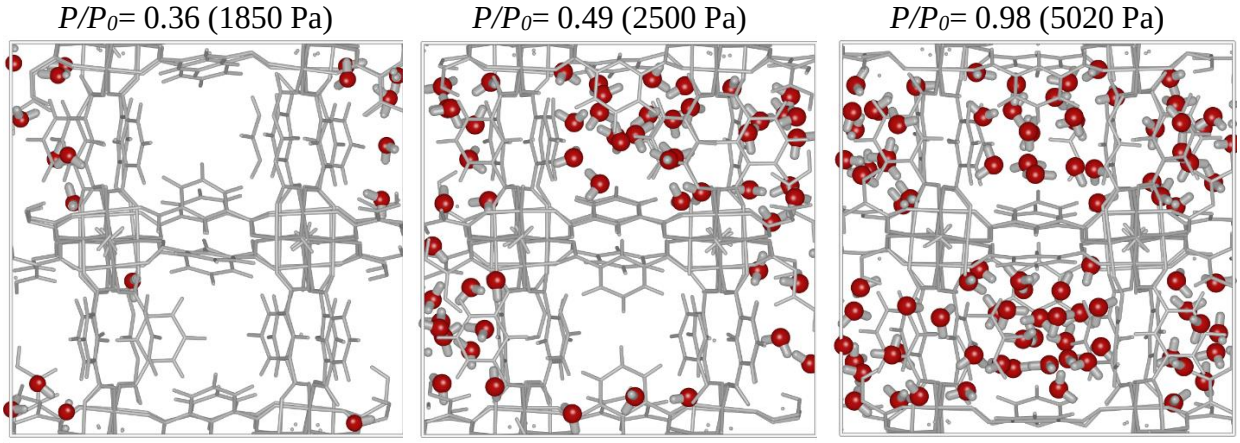

Figure S4. Simulation snapshots of water adsorption in flexible ideal CAU-10-H structure.

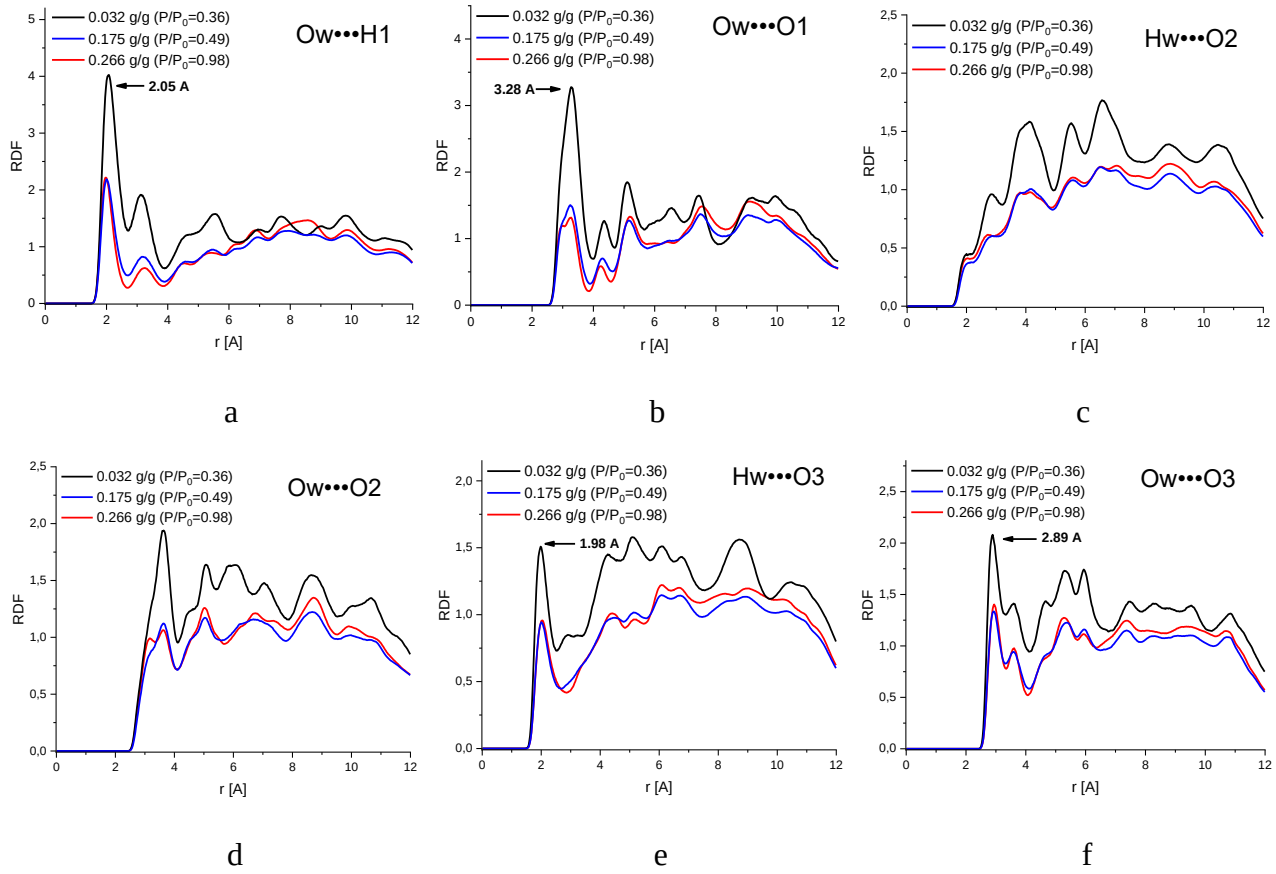

Figure S5. Radial distribution functions in flexible ideal CAU-10-H structure: Ow···H1 (a), Ow···O1 (b), Hw···O2 (c), Ow···O2 (d), Hw···O3 (e) and Ow···O3 (f).

Rigid uniform defective CAU-10-H structure

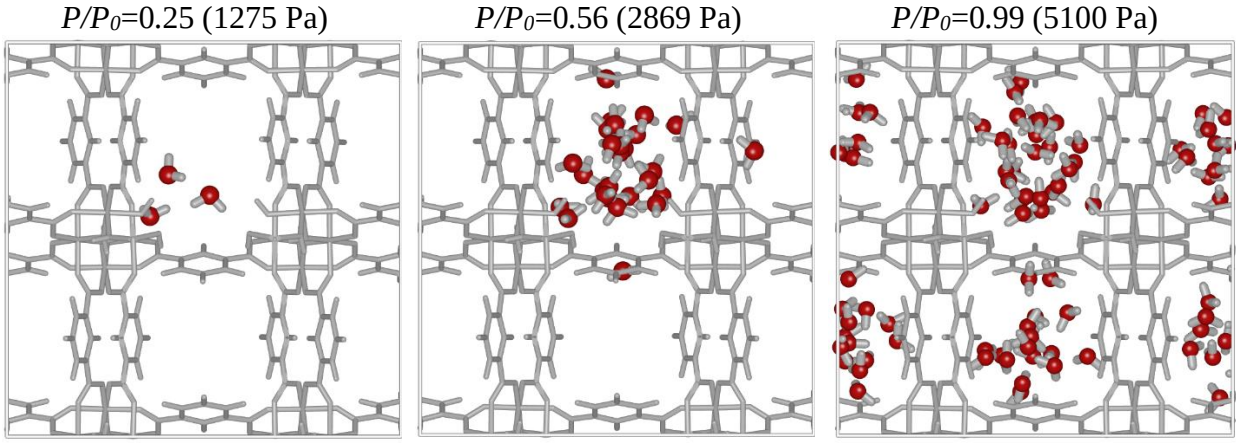

Figure S6. Simulation snapshots of water adsorption in rigid uniform defective CAU-10-H structure.

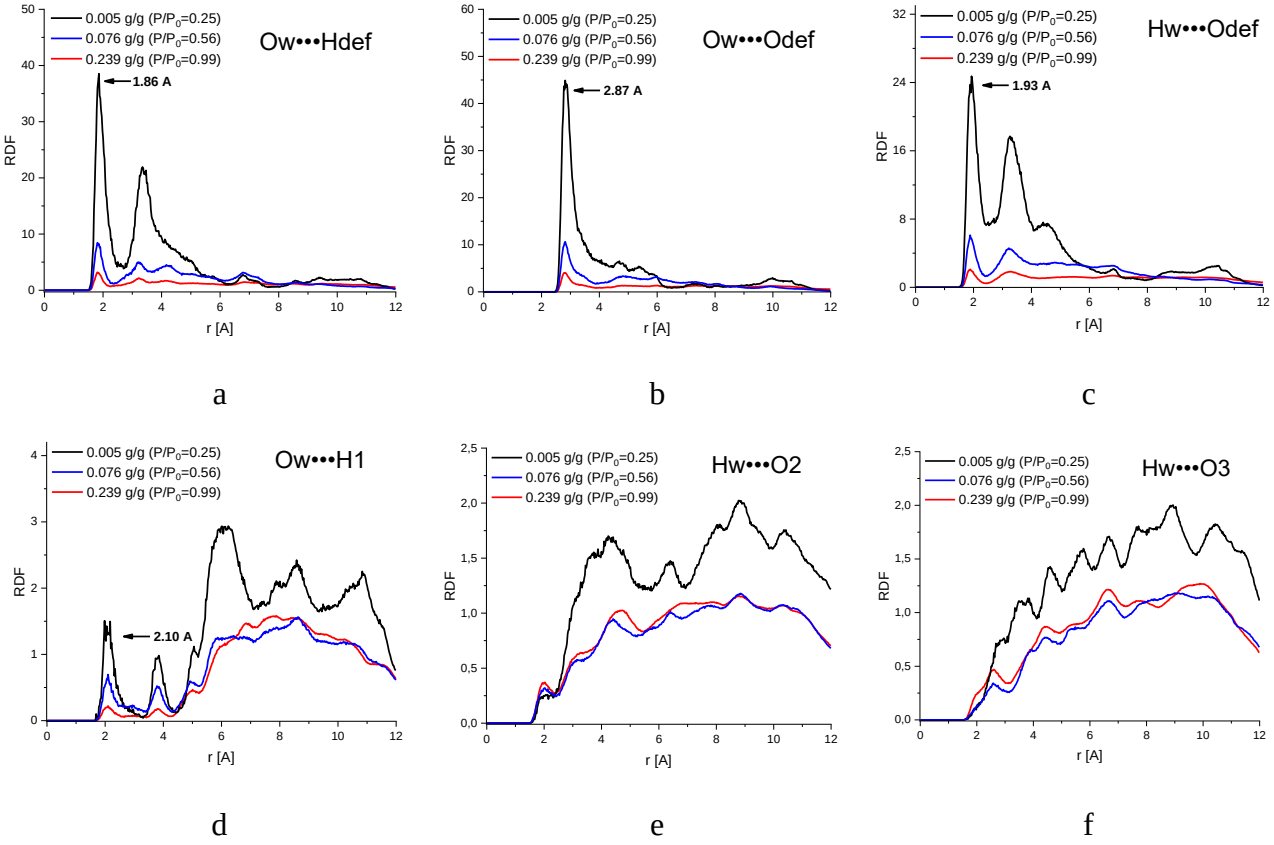

Figure S7. Radial distribution functions rigid uniform defective CAU-10-H structure: Ow···Hdef (a), Ow···Odef (b), Hw···Odef (c), Ow···H1 (b), Hw···O2 (e) and Hw···O3 (f).

Flexible mixed defective CAU-10-H structure

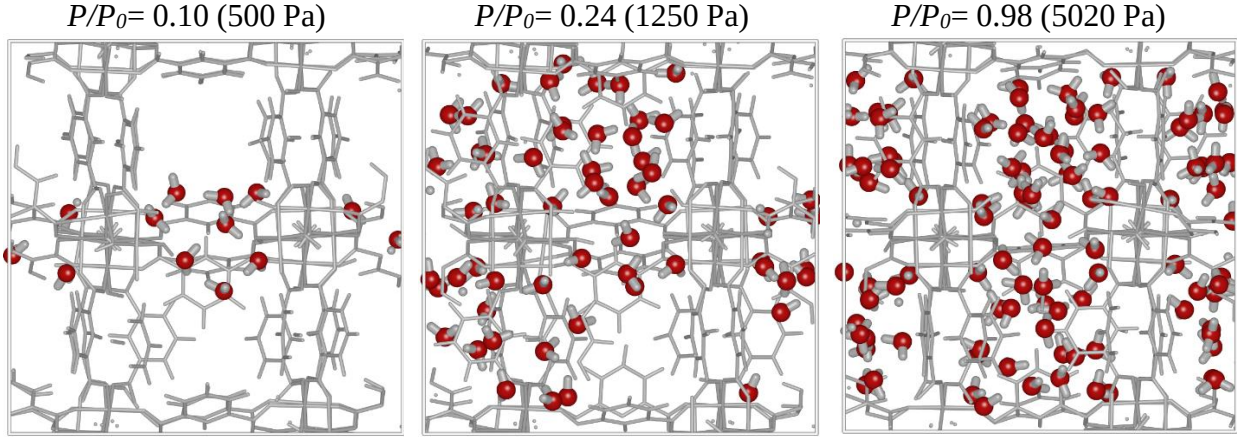

Figure S8. Simulation snapshots of water adsorption in flexible mixed defective CAU-10-H structure.

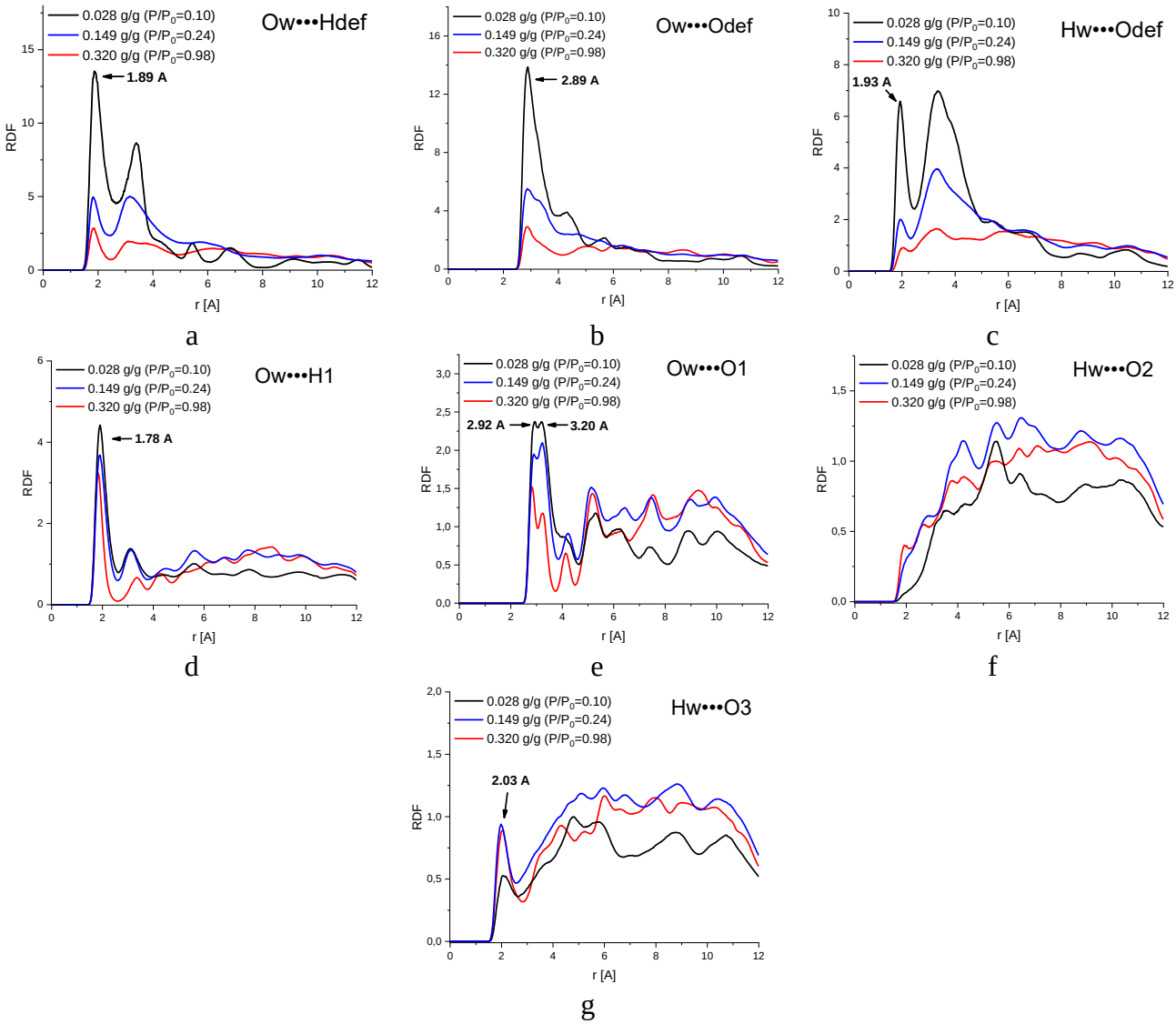

Figure S9. Radial distribution functions in flexible mixed defective CAU-10-H structure: Ow···Hdef (a), Ow···Odef (b), Hw···Odef (c), Ow···H1 (d), Ow···O1 (e), Ow···O2 (f) and Ow···O3 (g).

Section S6. Description of the linkers “flapping” motion

Snapshots generated during GCMC simulation for flexible ideal model of the CAU-10-H structure were analyzed to understand how the linker “flapping” motion depend on water loading. The angles between the reference (determined from the DFT calculations) and the current aromatic rings planes were calculated for each snapshot.

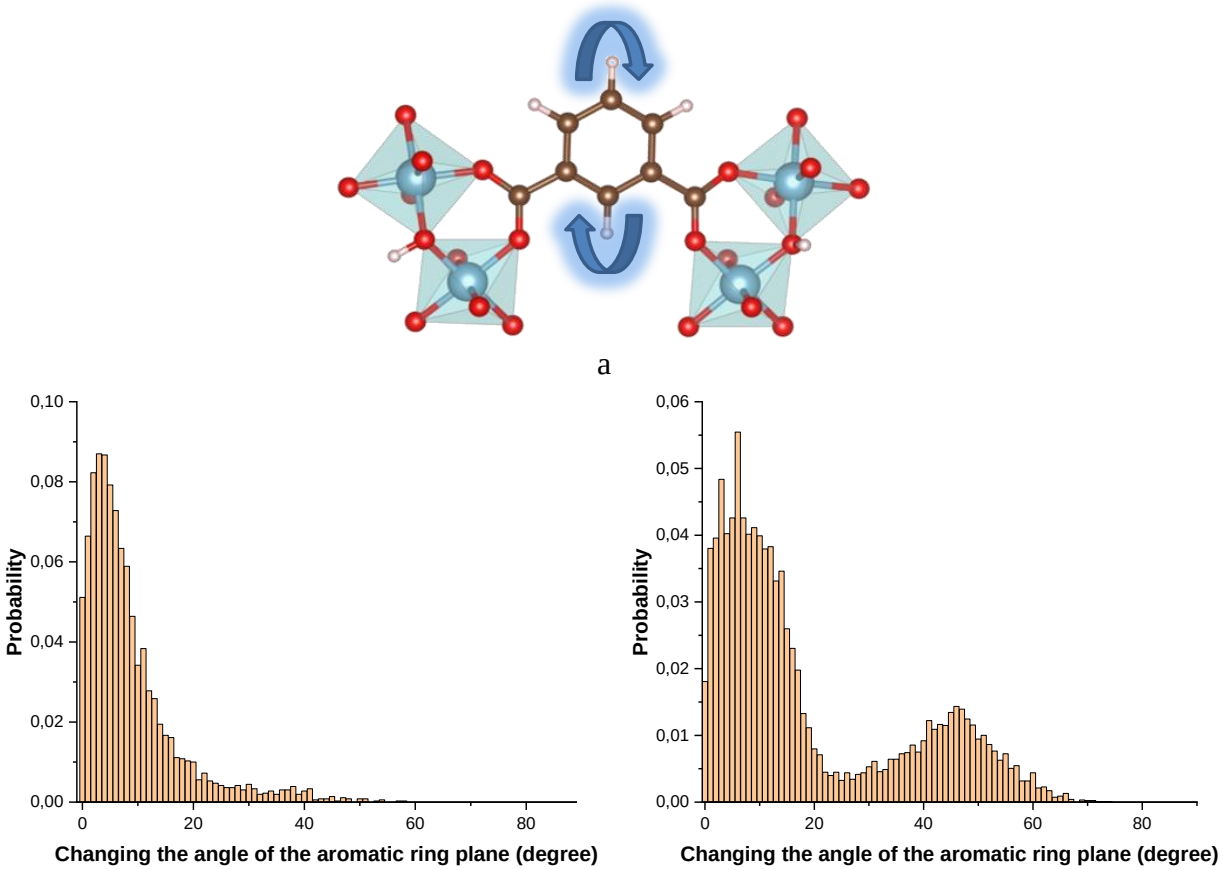

a

b

c

Figure S10. Schematic representation of the linker “flapping” motion (a). Dependence of the probability of changing the angle of the aromatic ring plane for the dry (b) and the water-loaded CAU-10-H at 0.266 g/g (c).

Section S7. Effect of force field parameters on simulated adsorption isotherms

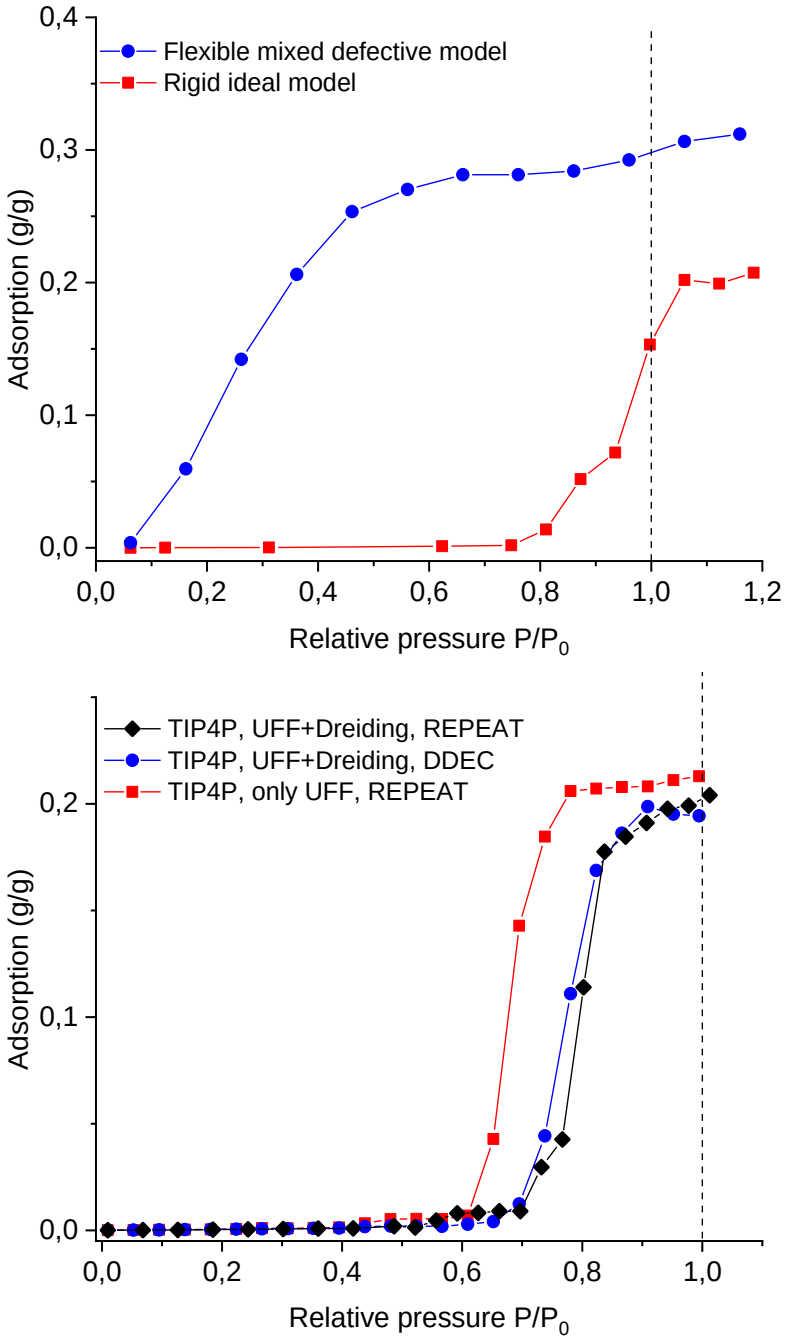

Figure S11. Top: Simulated adsorption isotherms in rigid ideal and flexible mixed defective models of the CAU-10-H structure at 300 K using the TIP4P/2005 water model. Bottom: Simulated adsorption isotherms in rigid ideal models of the CAU-10-H structure at 300 K using different Van der Waals interaction parameters and partial charges.

Section S8. Heats of adsorption

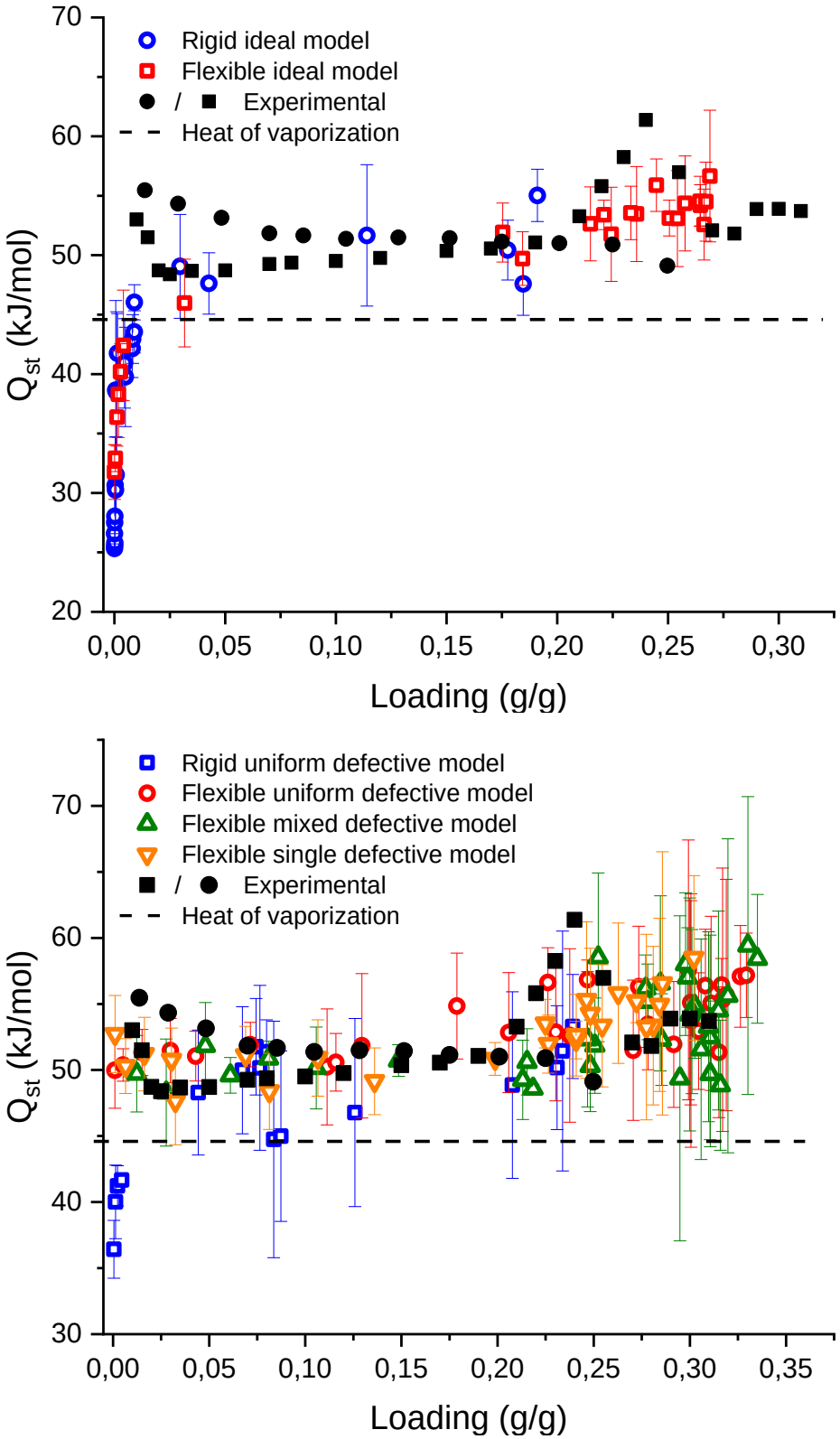

Figure S12. Experimental[26,27] and simulated heats of adsorption of TIP4P water in ideal (top) and defective (bottom) models of the CAU-10-H structure at 300 K.

Section S9. Nitrogen adsorption simulation

Theoretical values of the BET surface areas and micropore volumes for the ideal and defective MOF structures were obtained by simulation of the nitrogen adsorption at 77 K by the GCMC method. The sorbate-sorbate and sorbate-sorbent interaction were simulated as a sum of repulsion-dispersion and Coulombic interactions. The Lennard-Jones parameters and partial charges for the N_2 molecule were taken from the TraPPE force field[28]. In this force field a nitrogen molecule is simulated as a dumbbell with rigid distance between the atoms equal to 1.1 Å. An LJ site with parameters σ = 3.31 Å and ε/k_b = 36.0 K was located at the center of each nitrogen atom. The quadrupole moment of the N_2 molecule was simulated by three charges: two $-q$ charges, where q = 0.482 e, were located at the centers of the nitrogen atoms, and a $+2q$ charge was placed at the molecule center of mass. The force field parameters and partial charges of the ideal and defective CAU-10-H structures were similar to the ones used for simulation of the water adsorption (Section S3). However, hydrogen atoms in the structure were simulated using the LJ potential with parameters σ = 2.85 Å and ε/k_b = 7.65 K according to the Dreiding force field[29]. The simulation was performed using the structure fragment with the size of 2x2x4 unit cells, and the LJ interaction was shifted to zero at the cutoff radius 12.8 Å. The long-range electrostatic interactions were calculated using the Ewald summation technique. For each isotherm point, 60 000 cycles were performed for equilibration and 60 000 additional cycles were executed to determine the absolute adsorption value, n_{abs}. Each cycle consisted of N Monte Carlo steps, where N was equal to the number of adsorbate molecule but no less than 20. Translation, rotation, insertion and deletion moves were used as the Monte Carlo moves for the adsorbates. The Peng-Robinson equation of state was used to calculate fugacities and gas bulk densities, ρ_{bulk}, for each isotherm point. Excess adsorption, n_{excess}, was determined using the following formula:

$$n_{excess} = n_{abs} - V_{pore}\,\rho_{bulk} \qquad \text{S8}$$

Here V_{pore} is the MOF pore volume. Similar to the experimental measurement, the pore volume was measured by probing the structure with helium at room temperature. Void fractions, $V_{pore}/V_{structure}$, of the ideal and defective CAU-10-H structures were equal to 0.386 and 0.423, respectively.

Calculated excess adsorption isotherms for the ideal and defective structures are presented in Figures S12a and S12b. The range of pressures used for calculation of the BET surface areas was determined in accordance with the 'consistency criteria'[30] and is presented in Figures S12c and S12d. The adsorption isotherms in linear BET coordinates are presented in Figure S12e and S12f. The BET surface areas were equal to 685 m^2/g for the ideal unit cell and 793 m^2/g for

defective structure. The micropore volumes (V_{mic}) were determined from the excess adsorption at P/P_0 = 0.5 and were equal to 0.25 cm^3/g for the ideal structure and 0.29 cm^3/g for the defective one.

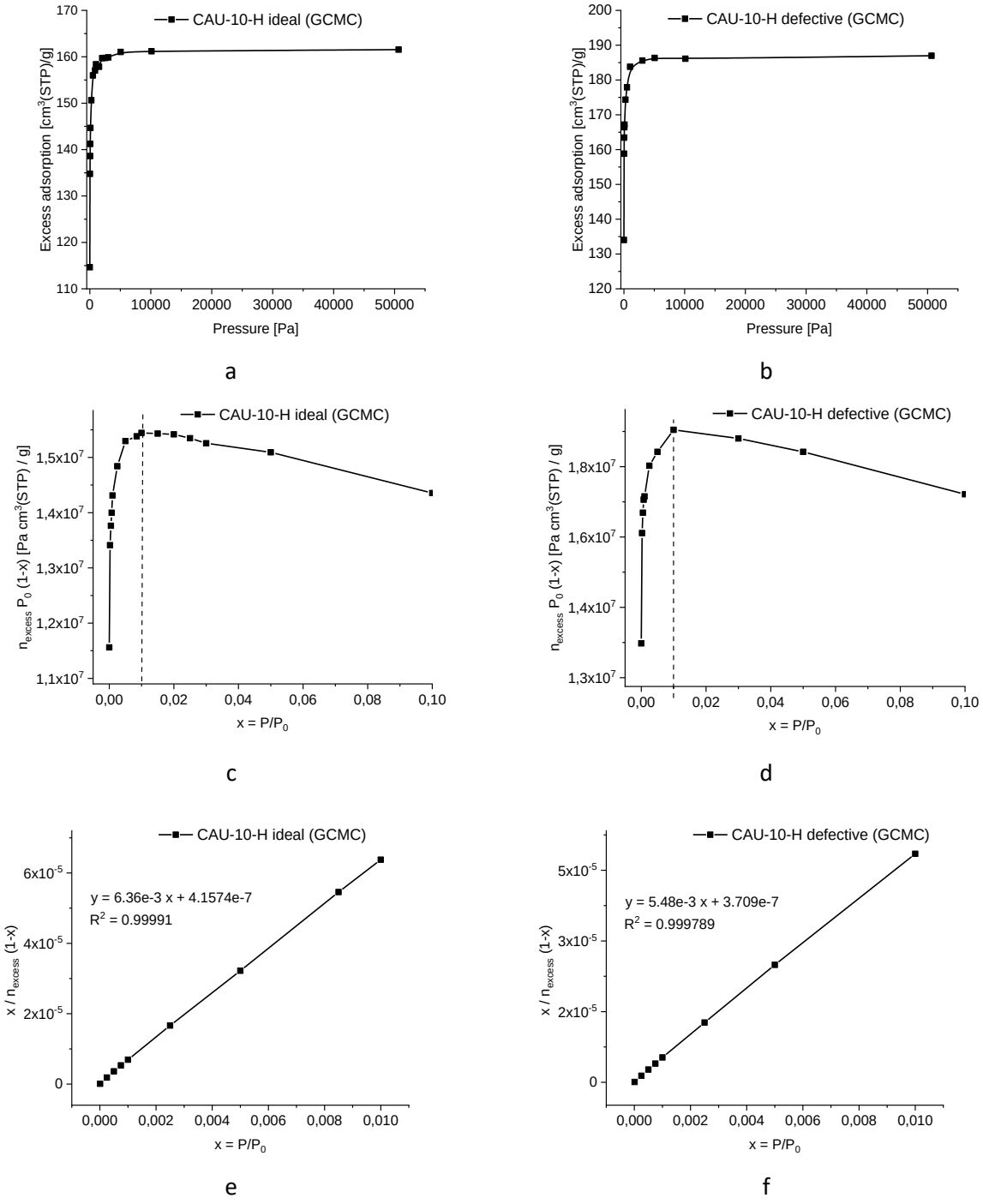

Figure S13. Simulated excess adsorption isotherm of N_2 at 77K for ideal (a) and defective (b) unit cells of CAU-10-H. A plot of $n_{excess}\ P_0\ (1 - P/P_0)$ vs P/P_0 for determining pressure range used to calculate the BET surface area for ideal (c) and defect (d) unit cells. BET linear plot satisfying both the first and second 'consistency criteria' for ideal (e) and defective (f) unit cells.

Section S10. Water adsorption isotherms on an absolute pressure scale

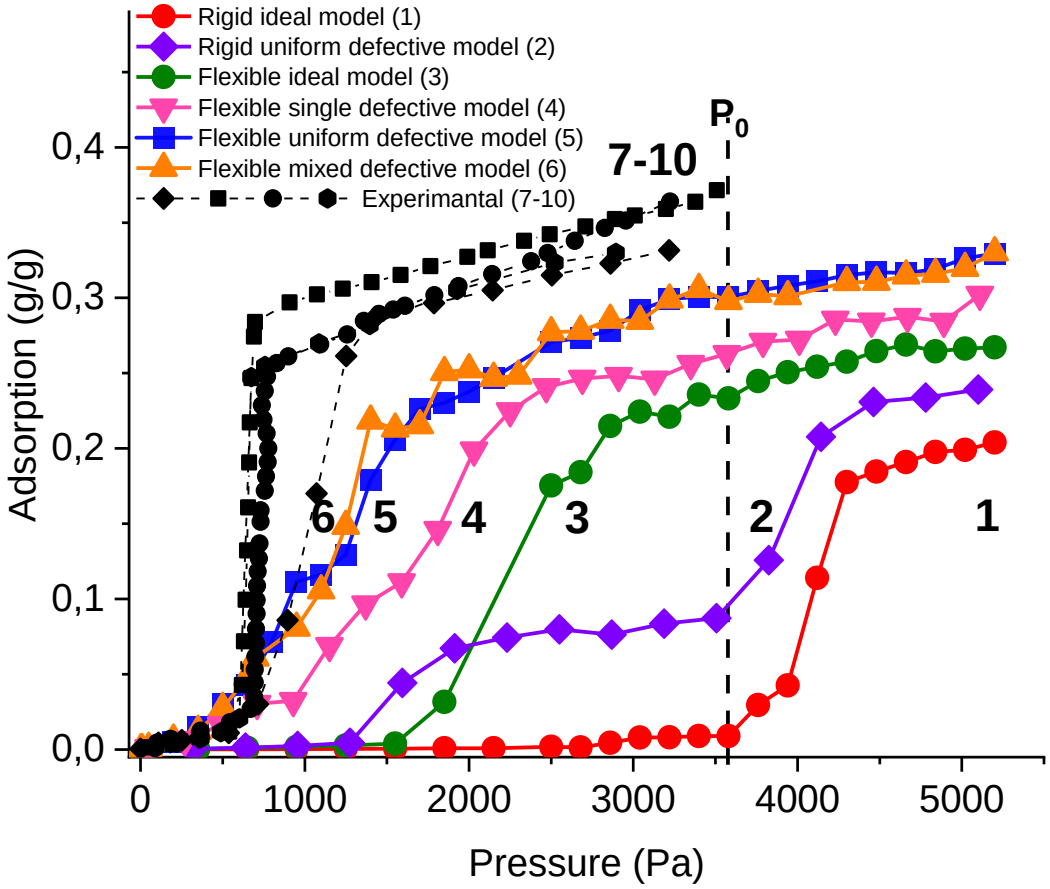

Figure S14. Water adsorption isotherms on an absolute pressure scale calculated by GCMC simulation for different models of the CAU-10-H structure and obtained from experiments[27,31–33]. Lines are a guide for the eye.

Section S11. Experimental TGA data for CAU-10-H

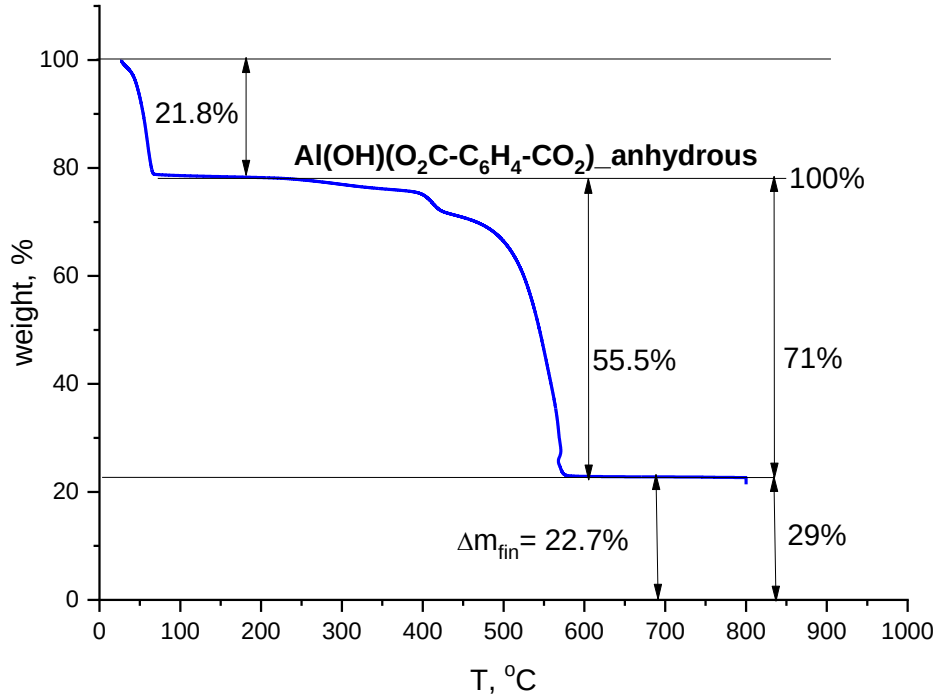

Figure S15. TGA-curve of CAU-10 measured in the air flow.

First weight loss at T < 100 °C is attributed to the dehydration of the synthesized CAU-10. The dehydrated material, corresponding to the range in the TGA curve of 300-400 °C, refers to a chemical formula per Al atom of Al(OH)(O_2C-C_6H_4-CO_2). Assuming that the final residual at high temperature is Al_2O_3 and taking the anhydrous Al(OH)(O_2C-C_6H_4-CO_2) weight as 100%, we expect a weight loss corresponding to the linker decomposition of 75.5%, and the residual Al_2O_3 of 24.5%. The experimental data exhibits a relative weight loss of about 71% with the residual weight of 29%. A lower weight loss at this stage indicates the presence of framework defects (linker vacancies).

Section S12. The pore size distribution

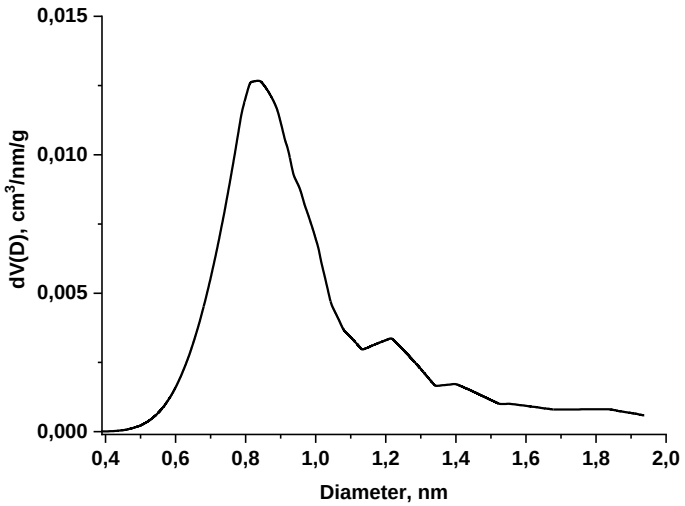

Figure S16. The pore size distribution calculated by the Horvath-Kawazoe method.

The pore size distribution was calculated by the Horvath-Kawazoe method based on nitrogen adsorption data from our previous work[27]. The results demonstrate that the main channel diameter is 0.83 nm, which is consistent with the average microchannel size determined from the CAU-10-H PXRD data. The pore size distribution also contains a second minor peak with an average channel size of 1.22 nm, which may indicate the presence of defects that lead to an increase in the channel size. In the case of a defective unit cell (Figure 1), the average size of a microchannel containing a defect increases and amounts to 1.03 nm.

References

1 G. Kresse and J. Hafner, Ab initio molecular dynamics for liquid metals, *Phys. Rev. B*, 1993, **47**, 558–561.
2 G. Kresse and J. Furthmüller, Efficient iterative schemes for ab initio total-energy calculations using a plane-wave basis set, *Phys. Rev. B*, 1996, **54**, 11169–11186.
3 P. E. Blöchl, Projector augmented-wave method, *Phys. Rev. B*, 1994, **50**, 17953–17979.
4 G. Kresse and D. Joubert, From ultrasoft pseudopotentials to the projector augmented-wave method, *Phys. Rev. B*, 1999, **59**, 1758–1775.
5 J. P. Perdew, K. Burke and M. Ernzerhof, Generalized Gradient Approximation Made Simple, *Phys. Rev. Lett.*, 1996, **77**, 3865–3868.
6 S. Grimme, Accurate description of van der Waals complexes by density functional theory including empirical corrections, *J. Comput. Chem.*, 2004, **25**, 1463–1473.
7 T. Bučko, J. Hafner, S. Lebègue and J. G. Ángyán, Improved Description of the Structure of Molecular and Layered Crystals: Ab Initio DFT Calculations with van der Waals Corrections, *J. Phys. Chem. A*, 2010, **114**, 11814–11824.
8 S. S. Tafreshi, A. Roldan and N. H. de Leeuw, Density Functional Theory Study of the Adsorption of Hydrazine on the Perfect and Defective Copper (100), (110), and (111) Surfaces, *J. Phys. Chem. C*, 2014, **118**, 26103–26114.
9 H. J. Monkhorst and J. D. Pack, Special points for Brillouin-zone integrations, *Phys. Rev. B*, 1976, **13**, 5188–5192.
10 C. Campañá, B. Mussard and T. K. Woo, Electrostatic Potential Derived Atomic Charges for Periodic Systems Using a Modified Error Functional, *J. Chem. Theory Comput.*, 2009, **5**, 2866–2878.
11 H. J. C. Berendsen, J. R. Grigera and T. P. Straatsma, The missing term in effective pair potentials, *J. Phys. Chem.*, 1987, **91**, 6269–6271.
12 W. L. Jorgensen, J. Chandrasekhar, J. D. Madura, R. W. Impey and M. L. Klein, Comparison of simple potential functions for simulating liquid water, *J. Chem. Phys.*, 1983, **79**, 926–935.
13 J. L. F. Abascal and C. Vega, A general purpose model for the condensed phases of water: TIP4P/2005, *J. Chem. Phys.*, 2005, **123**, 234505.
14 H. W. Horn, W. C. Swope, J. W. Pitera, J. D. Madura, T. J. Dick, G. L. Hura and T. Head-Gordon, Development of an improved four-site water model for biomolecular simulations: TIP4P-Ew, *J. Chem. Phys.*, 2004, **120**, 9665–9678.
15 M. W. Mahoney and W. L. Jorgensen, A five-site model for liquid water and the reproduction of the density anomaly by rigid, nonpolarizable potential functions, *J. Chem. Phys.*, 2000, **112**, 8910–8922.
16 S. W. Rick, A reoptimization of the five-site water potential (TIP5P) for use with Ewald sums, *J. Chem. Phys.*, 2004, **120**, 6085–6093.
17 M. F. De Lange, J.-J. Gutierrez-Sevillano, S. Hamad, T. J. H. Vlugt, S. Calero, J. Gascon and F. Kapteijn, Understanding Adsorption of Highly Polar Vapors on Mesoporous MIL-100(Cr) and MIL-101(Cr): Experiments and Molecular Simulations, *J. Phys. Chem. C*, 2013, **117**, 7613–7622.
18 P. G. M. Mileo, K. Ho Cho, J. Park, S. Devautour-Vinot, J.-S. Chang and G. Maurin, Unraveling the Water Adsorption Mechanism in the Mesoporous MIL-100(Fe) Metal–Organic Framework, *J. Phys. Chem. C*, 2019, **123**, 23014–23025.
19 P. Ghosh, K. C. Kim and R. Q. Snurr, Modeling Water and Ammonia Adsorption in Hydrophobic Metal–Organic Frameworks: Single Components and Mixtures, *J. Phys. Chem. C*, 2014, **118**, 1102–1110.
20 A. N. Gubkov, N. A. Fermor and N. I. Smirnov, Vapor Pressure of Mono-Poly Systems, *Zh. Prikl. Khim.*, 1964, 2204–2210.

21 O. C. Bridgeman and E. W. Aldrich, Vapor Pressure Tables for Water, *J. Heat Transf.*, 1964, **86**, 279–286.
22 V. Shen, D. Siderius, W.P. Krekelberg and H. W. Hatch, Standard Reference Simulation Website, NIST Standard Reference Database 173, 2020.
23 A. U. Ortiz, A. P. Freitas, A. Boutin, A. H. Fuchs and F.-X. Coudert, What makes zeolitic imidazolate frameworks hydrophobic or hydrophilic? The impact of geometry and functionalization on water adsorption, *Phys Chem Chem Phys*, 2014, **16**, 9940–9949.
24 H. Zhang and R. Q. Snurr, Computational Study of Water Adsorption in the Hydrophobic Metal–Organic Framework ZIF-8: Adsorption Mechanism and Acceleration of the Simulations, *J. Phys. Chem. C*, 2017, **121**, 24000–24010.
25 S. Paranthaman, F.-X. Coudert and A. H. Fuchs, Water adsorption in hydrophobic MOF channels, *Phys. Chem. Chem. Phys.*, 2010, **12**, 8123.
26 D. Fröhlich, E. Pantatosaki, P. D. Kolokathis, K. Markey, H. Reinsch, M. Baumgartner, M. A. van der Veen, D. E. De Vos, N. Stock, G. K. Papadopoulos, S. K. Henninger and C. Janiak, Water adsorption behaviour of CAU-10-H: a thorough investigation of its structure–property relationships, *J. Mater. Chem. A*, 2016, **4**, 11859–11869.
27 M. V. Solovyeva, A. I. Shkatulov, L. G. Gordeeva, E. A. Fedorova, T. A. Krieger and Y. I. Aristov, Water Vapor Adsorption on CAU-10-X : Effect of Functional Groups on Adsorption Equilibrium and Mechanisms, *Langmuir*, 2021, **37**, 693–702.
28 J. J. Potoff and J. I. Siepmann, Vapor–liquid equilibria of mixtures containing alkanes, carbon dioxide, and nitrogen, *AIChE J.*, 2001, **47**, 1676–1682.
29 S. L. Mayo, B. D. Olafson and W. A. Goddard, DREIDING: a generic force field for molecular simulations, *J. Phys. Chem.*, 1990, **94**, 8897–8909.
30 J. Rouquerol, P. Llewellyn and F. Rouquerol, Is the BET equation applicable to microporous adsorbents?, *Stud. Surf. Sci. Catal.*, 2007, **160**, 49–56.
31 D. Lenzen, P. Bendix, H. Reinsch, D. Fröhlich, H. Kummer, M. Möllers, P. P. C. Hügenell, R. Gläser, S. Henninger and N. Stock, Scalable Green Synthesis and Full-Scale Test of the Metal-Organic Framework CAU-10-H for Use in Adsorption-Driven Chillers, *Adv. Mater.*, 2018, **30**, 1705869.
32 V. B. López-Cervantes, E. Sánchez-González, T. Jurado-Vázquez, A. Tejeda-Cruz, E. González-Zamora and I. A. Ibarra, CO2 adsorption under humid conditions: Self-regulated water content in CAU-10, *Polyhedron*, 2018, **155**, 163–169.
33 S. Leubner, R. Stäglich, J. Franke, J. Jacobsen, J. Gosch, R. Siegel, H. Reinsch, G. Maurin, J. Senker, P. G. Yot and N. Stock, Solvent Impact on the Properties of Benchmark Metal–Organic Frameworks: Acetonitrile-Based Synthesis of CAU-10, Ce-UiO-66, and Al-MIL-53, *Chem. – Eur. J.*, 2020, **26**, 3877–3883.